Investigation of MEMS micro-implants: *in vitro* and *in vivo* analysis for advanced biomedical applications

BALOGH-LANTOS Zsófia

PhD Supervisors:

Dr. HORVÁTH Ágoston Csaba, PhD

Dr. IVÁN Kristóf, PhD

Theses of the PhD Dissertation

Pázmány Péter Catholic University

Roska Tamás Doctoral School of Sciences and Technology

Budapest, 2025

1 Introduction

The brain is the body's most complex and vital organ, responsible for controlling cognitive functions, emotions, motor skills, and autonomic processes. Despite its remarkable adaptability, the brain remains vulnerable to a variety of diseases, including neurodegenerative and neurological diseases, as well as disorders affecting glial cells and tumors. Diseases, including Alzheimer's disease [1], Parkinson's disease [2], and epilepsy [3], have a significant impact on the quality of life of individuals and place a growing burden on healthcare systems around the world [4]. Neurodegenerative and neurological diseases often result from a combination of genetic, environmental, and lifestyle factors that contribute to neuronal damage and dysfunction. These diseases can result in progressive neuronal loss, impaired neurotransmission, and inflammation, leading to severe cognitive and motor impairments [5]–[7]. Studying the underlying mechanisms of these disorders not only improves our understanding of brain function, but also opens avenues for novel therapeutic interventions.

Brain diseases pose a growing challenge to modern healthcare, with neurodegenerative and psychiatric disorders demanding innovative neuromodulation strategies beyond traditional pharmacological treatments. While electrical stimulation has shown clinical success and optogenetics have advanced neuroscience research, infrared neural stimulation (INS) is emerging as a promising alternative due to its non-invasive nature and ability to modulate neural activity without genetic modifications [8]. Research has linked INS effects to mechanosensitive ion channels, particularly Transient Receptor Potential Vanilloid (TRPV) channels, which play a key role in neural excitability and disease pathology [9]. Despite progress, the mechanisms of INS remain under investigation, with studies revealing both excitatory and inhibitory effects [10]. Our research group has developed a photonic implantable device to deliver infrared (IR) irradiation while recording neural activity and tissue temperature, demonstrating reversible excitation and suppression of cortical neurons in rats without heat-induced cell loss [11]. The second part of this study focuses on infrared neurostimulation, where high-density laminar electrode recordings were used to examine the effects of pulsed (PW) and continuous-wave (CW) infrared stimulation on cortical neurons in anesthetized rats. The results revealed that IR stimulation produces layer- and cell-type-specific effects, with pulsed stimulation enhancing neuronal firing and continuous stimulation suppressing activity. These findings provide valuable insights into the biophysical mechanisms underlying INS and highlight its potential as a powerful tool for targeted neuromodulation in neurological disorders.

A significant advancement in the field of neuroscience research is the development of microimplants for neural recording and intervention. These devices, often incorporating

microelectrode arrays or multimodal biosensors, enable researchers to monitor neural activity with remarkable temporal and spatial precision. Their ability to detect the electrical signals of individual neurons or neural networks is a crucial advantage, allowing for the identification of pathological patterns linked to various neurological disorders. Despite the advances made in the field, conventional electrode materials continue to exhibit several limitations. Traditional metal-based electrodes, while effective for recording neural activity, have been observed to cause immune responses, scar tissue formation, and signal degradation over time [12]. Furthermore, their opacity hinders the integration of electrophysiology with optical imaging techniques, limiting the ability to visualize neural circuits in action. To overcome these challenges, researchers are developing biocompatible, flexible, and optically transparent microelectrode arrays. Integrating electrophysiology with two-photon imaging provides complementary spatial and temporal information, allowing for a deeper understanding of neuronal connectivity and activity. The first part of this research focused on evaluating the optical properties and long-term spike detection performance of a transparent, flexible microelectrocorticography (microECoG) device made from thiol-ene/acrylate shape memory polymer (SMP). This device is designed for compatibility with two-photon microscopy, enabling simultaneous optical imaging and electrophysiological recording. The results indicate that the device does not introduce significant optical distortion and allows reliable single-unit spike detection over extended periods, up to at least seven weeks. By demonstrating its stability for long-term neural monitoring, this study contributes to the advancement of minimally invasive neurotechnologies for chronic multimodal studies.

By integrating advanced neurotechnologies for both neural recording and modulation, this research provides new avenues for studying brain function and developing therapeutic strategies. The findings contribute to the refinement of neurotechnological tools, offering new possibilities for precise and minimally invasive interventions in neurological disorders.

Thesis group I.

I used high-density laminar electrophysiological recordings with a Neuropixels probe to examine the intracortical response to pulsed and continuous-wave infrared irradiation in adult Wistar rats ($n = 8$). In this study, I recorded the activity of 7,549 single-units from anesthetized rats during pulsed (1 Hz, 10 Hz, 50 Hz, 100 Hz, 500 Hz) and continuous-wave infrared light stimulation. The stimulation was applied using an optrode device positioned in layer 5 of the somatosensory cortex. I focused on investigating the effects of the stimulation on the firing rate of cells across different cortical layers and cell types, as well as exploring the temporal dynamics of the neuronal response.

The publication related to this thesis group is: [J1]
The conference posters related to this thesis group are: [P1]–[P3]

Thesis I.1 *I showed that continuous-wave infrared stimulation leads to a greater proportion of cortical neurons exhibiting suppressed firing compared to pulsed wave stimulation, which more commonly induced increased activity. Neurons with increased firing rates nearly doubled their activity during stimulation, while suppressed neurons exhibited an average reduction of about 40%. Additionally, CW stimulation induced significantly larger changes in firing rates than pulsed wave stimulation across the tested frequencies.*

This study combines a photonic microtool with high-density electrophysiological recordings to analyze the response of cortical principal cells and interneurons to infrared stimulation in anesthetized rats. Continuous wave and pulsed IR irradiation were used to investigate response differences along cortical layers. Experiments were conducted on eight adult Wistar rats (5 females), with spikes detected using KiloSort3 and manually curated based on waveform characteristics and quality metrics (presence ratio, ISI violations, amplitude cutoff) calculated in SpikeInterface. For each single unit, the relative firing rate change compared to the baseline period was calculated in ten-second intervals for every ON (stimulation, IR light turned on) period as shown in Equation 1.1.

$$RelativeFiringRate = \frac{FiringRate - Baseline}{Baseline} \tag{1.1}$$

The baseline firing rate was defined as the average firing rate during the last two minutes of OFF periods (spontaneous cortical activity) preceding the ON periods (IR stimulation-related activity). To ensure data quality, single units were also filtered based on the baseline firing rate. A threshold was set according to the distribution of baseline data. Specifically, the lower threshold was set as $10th\ percentile - 3 \times$

interpercentile range, where the interpercentile range is calculated as the difference between the 90th and 10th percentiles. The upper threshold was defined similarly as $90th\ percentile + 3 \times interpercentile\ range$. The application of these thresholds allowed the exclusion of extreme values, with approximately 4 % ($n = 322$) of the data being identified and removed as outliers.

To examine the impact of stimulation, each single unit was classified based on the relative firing rate change as having either suppressed, increased, or neutral activity (unaffected). This categorization was determined through the assessment of the degree of change in the firing rate. A single unit was classified as excited (increased activity) if its firing rate increased more than 20% compared to the baseline during at least 60% of the ON periods, suppressed if its firing rate decreased by 20% or more, and unaffected if the firing rate fell within the range of -20% to 20%. To analyze differences between multiple groups, one-way ANOVA and Kruskal-Wallis tests (with significance level $p < 0.05$) were performed with GraphPad software (Prism v.9.5.1). When the overall model exhibited significance, Dunnett's test, Dunn's test, and Tukey's test were employed as post-hoc tests for parametric and non-parametric analyses, respectively, to evaluate specific group differences. Post hoc tests, Dunnett's for comparing to control and Tukey's for comparing each value to each other, were used to handle multiple comparisons in ANOVA. Dunn's tests were used to determine significant differences between groups after obtaining a significant result from the overall model for Kruskal-Wallis tests.

Figure 1.1A illustrates the percentage of neurons falling into each category across different stimulation protocols. The firing rate of the majority of single units did not change markedly throughout the entirety of the infrared stimulation protocol, except when continuous wave stimulation was applied. In cases where cells were affected, pulsed wave stimulation elicited a greater number of single units with increased activity compared to those with decreased activity. Conversely, continuous wave stimulation elicited a greater proportion of single units showing activity suppression. Figure 1.1B and C present the average change in firing rate for single units exhibiting either suppressed or increased activity. Single units that were activated by IR stimulation doubled their firing rates on average compared to the baseline firing rates, while suppressed units showed about a 40% decrease in their firing rates. Those single units that increased their activity to stimulation exhibited significantly higher firing rate changes exposed to CW stimulation than to pulsed stimulation (1 Hz, 10 Hz, 50 Hz)(Kruskal-Wallis test: $p < 0.0001$). Single units with suppressed activity exhibited a significantly lower firing rate during CW stimulation in comparison to stimulation at frequencies of 1 Hz, 10 Hz, and 50 Hz (Kruskal-Wallis test: $p < 0.0001$).

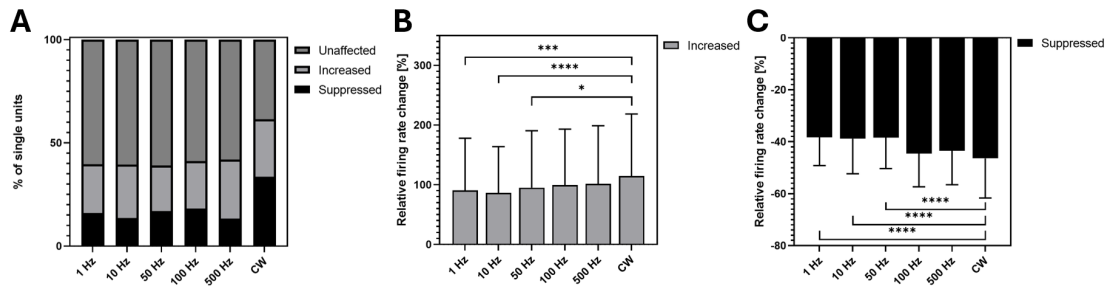

Figure 1.1: Effects of infrared stimulation on firing rates. A) The percentage of single units with suppressed and increased activity and unaffected cells at each infrared stimulation frequency. The average relative change of the firing rate in cells with B) increased and C) suppressed activity. There is a significant difference between CW stimulation and 1 Hz, 10 Hz, and 50 Hz stimulation for both single units with increased and suppressed activity. Error bars represent standard deviation. (Kruskal-Wallis test: $*p < 0.05, ***p < 0.001, ****p < 0.0001$)[J1].

Thesis I.2 *I determined that the effect induced by continuous infrared stimulation depends on which cortical layer is examined. I observed significantly greater suppression in the superficial and input layers (layers 2/3/4) compared to the deeper layers (layers 5 and 6).*

The laminar position of Neuropixels probe recording sites was determined using cortical population activity and Nissl-stained brain sections. Layer 1 was excluded due to sparse single units. Layers 2, 3, and 4 were grouped due to boundary uncertainties and low neuronal activity under anesthesia ($\sim 650\ \mu m$ thick). Layer 5 ($\sim 450\ \mu m$) contained large pyramidal cells and exhibited the strongest activity, while Layer 6 ($\sim 600\ \mu m$) showed weaker firing and was distinguished from white matter by reduced activity and short-duration spikes. Single units were assigned to layers based on the site where their spike waveform had the largest amplitude. Depth normalization was applied across animals following established literature, adjusting layers to a 0–3 depth scale, later normalized between 0–1 for visualization.

During pulsed wave stimulation, most single units remained unaffected across all layers (Superficial/Input: 63.54%, Layer 5: 61.92%, Layer 6: 63.71%). Continuous-wave (CW) stimulation, however, significantly increased the proportion of affected cells, particularly those with suppressed activity (Superficial/Input: 47.83%, Layer 5: 35.82%, Layer 6: 23.72%).

Firing rate changes were most pronounced during CW stimulation, with a significant increase in activity in superficial/input layers and Layer 5 (Kruskal-Wallis: p=0.0106, p<0.0001). Suppressed units showed a significant decrease in firing rate across all layers during CW stimulation compared to lower frequencies (p=0.0004 to p<0.0001). Layer 6 had fewer suppressed units, with more cells showing increased activity. Figure 1.2 illustrates that suppressed units were concentrated in superficial/input layers and Layer 5, units with increased activity in layer 6, while unaffected cells remained the majority in all layers.

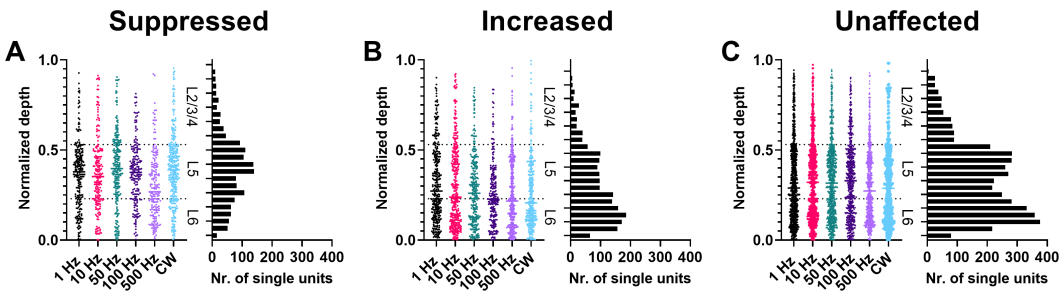

Figure 1.2: Responses of single units with suppressed A), increased B) and unaffected C) responses to infrared neural stimulation at different frequencies, plotted by cortical depth. Each point represents a single unit. The y-axis indicates the normalized depth of the neurons, with dashed lines marking the boundaries between layers. Alongside each subplot is a distribution plot along the y-axis, depicting the spread of neurons' depths for each response category [J1].

Thesis I.3 *I determined that the stimulation frequency significantly influences the activity of interneurons and principal cells: at higher stimulation frequencies, activity increased in the excited cells and decreased in the suppressed cells. In the case of interneurons, more cells showed suppressed activity, while in the case of principal cells, increased activity was observed in the majority of cells.*

Neocortical neurons are classified as excitatory principal cells or inhibitory interneurons based on extracellular spike duration. Shorter spikes indicate interneurons, while longer spikes correspond to principal cells. To distinguish these types, I calculated the trough-to-peak time for each unit. The distribution was bimodal (Hartigan's dip test, p=0.0046), confirming two distinct groups. Since distributions varied across animals, thresholds were manually set per animal (ranging from 0.41–0.61 ms). Units with trough-to-peak times above the threshold were classified as principal cells, while those at or below were identified as interneurons.

Next, for each stimulation type, I determined the proportion of putative interneurons and principal cells exhibiting suppressed or increased activity. I have found that the activity of more interneurons was suppressed ($23.17\% \pm 13.2\%$) than increased ($20\% \pm 10.11\%$), whereas more principal cells showed increased activity ($27.85\% \pm 9.91\%$) compared to suppressed activity ($12.98\% \pm 9.45\%$) (Figure 1.3A-D). The percentage of interneurons and principal cells, whether suppressed (Figure 1.3A and C) or exhibiting increased activity (Figure 1.3B and D), appeared to increase with stimulation frequency. However, a statistically significant difference was found only for suppressed interneurons between 500 Hz, 10 Hz, and 1 Hz stimulation compared to CW stimulation (Kruskal-Wallis test: $p = 0.0076$). In conclusion, the examination of the types of neurons revealed that interneurons exhibited a greater degree of suppressed activity than increased activity, especially at 50 Hz, 100 Hz, and CW stimulation, while principal cells exhibited the opposite pattern, with a greater number of cells showing increased activity than suppressed activity. The firing rate changes also exhibited distinct patterns. For principal cells, higher stimulation frequencies appeared to amplify the existing response pattern: those

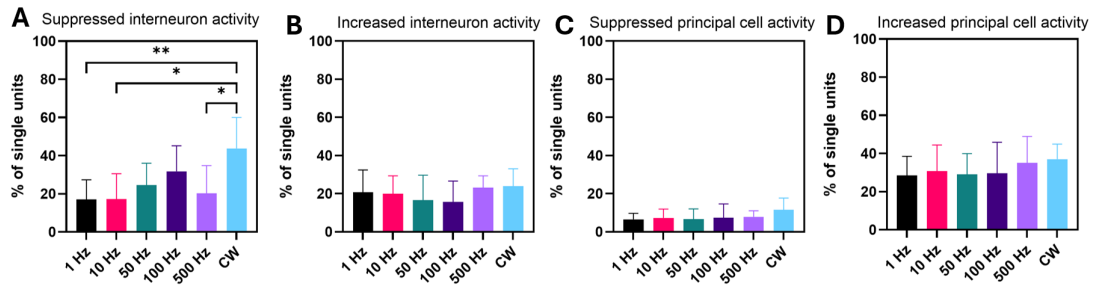

Figure 1.3: Effects of infrares stimulation on interneurons and principal cells. A) Percentage of suppressed interneurons. There is a statistically significant difference in the number of interneurons that are suppressed between the stimulation of 1 Hz, 10 Hz, 500 Hz, and CW stimulation. B) Percentage of interneurons with increased activity. C) Percentage of suppressed principal cells. D) Percentage of principal cells with increased activity. Error bars represent standard deviation. (Kruskal-Wallis test: $*p < 0.05, **p < 0.01$) [J1].

with increased activity tended to show progressively higher firing rates, while those with suppressed activity showed progressively greater reductions in firing. In the case of interneurons, there was no significant increase or decrease. Nevertheless, the modulatory effect appeared to be most pronounced during continuous wave stimulation, associated with the highest relative firing rates in interneurons showing enhanced activity and the lowest in those showing suppression.

Thesis I.4 *I showed that in the case of continuous infrared stimulation, the rise time of the firing rate was significantly longer than in the case of pulsed stimulation. The fall times were consistently faster in comparison. This points to the unique temporal dynamics of neural responses to heating. The rise time remained consistent across the five stimulation periods.*

Investigating the temporal relationship between infrared stimulation-induced temperature changes and neuronal firing rate responses is crucial, given the limited discussion of this aspect in the literature. Analyzing the changes in neuronal activity during suppression and excitation, and investigating how these dynamics correlate with the corresponding thermal effects, may provide new insights into infrared neural stimulation and facilitate the design of optimized stimulation protocols. Figure 1.4 shows these response times across stimulation frequencies and stimulation trials. The time required to reach 90% of the maximum cortical temperature during the ON period (rise time) for each stimulation frequency shows a consistent increase with higher stimulation frequencies (Figure 1.4A). The rise times of the relative firing rate for suppressed single units during the first ON period (Figure 1.4A) were significantly longer with CW stimulation compared to pulsed infrared light (Kruskal-Wallis test: $p = 0.0007$). The data also showed that single units with increased activity had a significantly longer rise time with CW stimulation compared to 50 Hz stimulation (Kruskal-Wallis test: $p = 0.0002$).

I also examined the rate of change of temperature and firing rate after the stimulation trials. Figure 1.4B shows the time taken to reach 10% of the maximum temperature after

the light was turned off (fall time). Interestingly, the fall time of the temperature did not show significant variation across different stimulation frequencies, and in particular, it was considerably faster than the rise times of the temperature (as shown in Figure 1.4A). The time taken to reach 10% of the mean change in firing rate during the first OFF period was also examined. It can be noted that the fall time was shorter during CW stimulation compared to pulsed wave stimulation in both single units, with increased and suppressed activity. In the case of single units with increased activity, the results indicated that the fall time was significantly shorter during CW stimulation compared to 10 and 50 Hz stimulation (Kruskal-Wallis test: $p = 0.0094$). However, for suppressed single units, there was no significant difference in fall times, although CW stimulation still resulted in the shortest fall time.

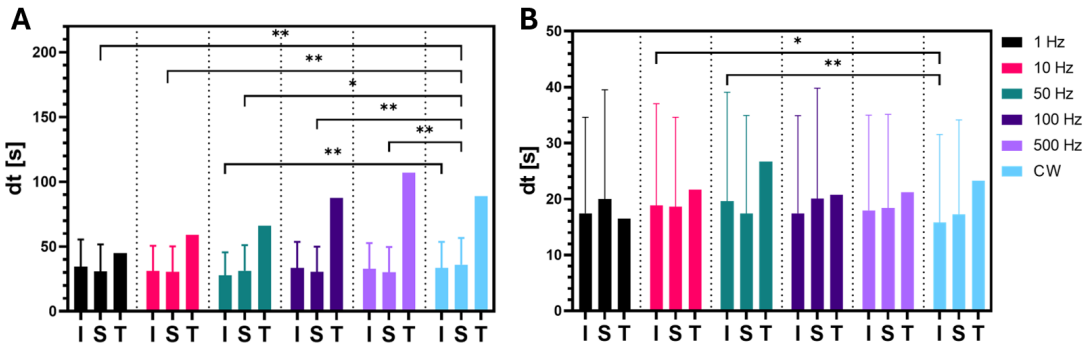

Figure 1.4: Single unit rise and fall times. A) The rise time of single units with increased (I) and suppressed (S) activity during the first stimulation trial, at every stimulation frequency. The rise time was significantly longer when single units were stimulated with continuous light than with 50 Hz stimulation. (T) The time needed for the cortical temperature to reach 90% of the maximum at each IR stimulating frequency from the onset of the stimulus, calculated from one measurement. B) The fall time of increased (I) and suppressed (S) activity after the first stimulation trial. The fall time was significantly shorter when single units were stimulated with continuous light than with 10 Hz and 50 Hz stimulation. Error bars represent standard deviation. (Kruskal-Wallis test:$*p < 0.05, **p < 0.01$) [J1].

Thesis group II.

A transparent microECoG device was presented using thiol-ene/acrylate shape memory polymer as a biocompatible flexible transparent polymer substrate and Parylene C encapsulating material with gold and SIROF as a conductive layer. This array features 115 μm diameter recording sites, which are spaced 400 μm apart. I assessed the impact of an SMP-based microECoG device on two-photon imaging by analyzing fluorescent microbeads and hippocampal slices in *in vitro* images, and the relative fluorescent intensity change in mice somatosensory (n=3) cortex *in vivo*. I also explored the SMP microECoG's ability to record single-unit activity from the mice hippocampus (n=7) over extended periods.

The publications related to this thesis group are: [J2], [J3]
The conference posters related to this thesis group are: [P4], [P5]

Thesis II.1 *Using fluorescent microbeads, I showed that the SMP-based microECoG device produces no significant optical distortion on two-photon microscopy images. Additionally, dendritic diameters in hippocampal slices remained consistent across imaging depths, indicating that fine neuronal structures can be visualized with high fidelity through the device, preserving the optical clarity required for high-resolution, multimodal imaging.*

Transparent shape memory polymers (SMPs), such as thermoset thiol-ene/acrylate, exhibit stiffness at room temperature but become flexible at body temperature. This thermal responsiveness makes surgical implantation easier by allowing the material to soften in situ, minimising tissue damage. Once implanted, it transitions from 1 GPa to 18 MPa with minimal fluid absorption ($< 0.3\%$), ensuring stability [13]. A thiol-ene/acrylate-based microelectrocorticography device was fabricated via spin-coating, enabling precise control over thickness. The 18 μm thick device, with 31 conductive channels, was produced at Qualia Labs, Inc. and packaged at Pázmány Péter Catholic University.

To assess optical distortion, two-photon imaging was conducted using 6 μm fluorescent beads sealed between glass slides. Imaging was done with and without the device, ensuring consistent focal depth while evaluating transparency. Bead detection and size analysis were performed using MATLAB scripts, employing adaptive and global thresholding based on intensity levels. Circular Hough Transform was used to identify bead centers and radii, ensuring robustness against noise and variations in illumination. Statistical analysis, including mean diameter and standard deviation, was conducted in MATLAB,

while bead size comparisons were performed using Student's paired t-test ($\alpha = 0.05$) in OriginPro.

Figure 1.5A shows box plots of bead diameters, with values normalized to the mean diameter observed in the absence of the device ($5.6651 \pm 0.0066\ \mu m$). A Student's paired t-test was performed at a significance level of 0.05 and the results showed no significant difference in bead diameters between the two conditions ($t(67) = 1.08$, $p = 0.29$, mean difference: $0.0142\ \mu m$). These results support my hypothesis that the SMP-based microECoG device does not introduce significant optical distortion. Overall, the bead size measurements remained consistent with and without the device and closely matched the nominal bead size, indicating that the resolution limit of the imaging system, rather than the presence of the device, is the primary factor affecting accuracy.

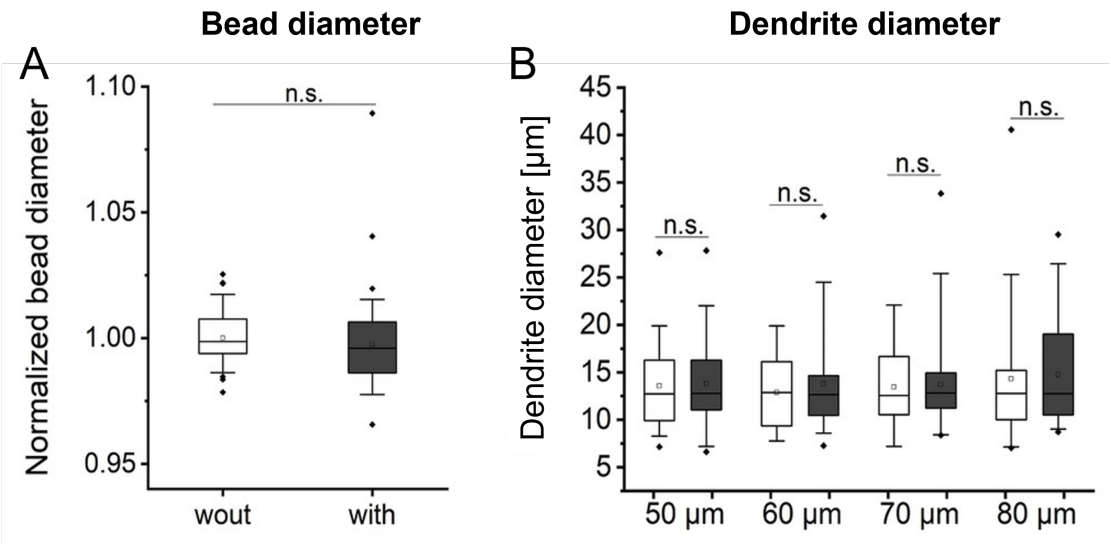

Figure 1.5: Diameter of the beads and dendrites. A) Normalized diameter of the same beads without (n = 68) and with (n = 68) the microECoG device covering them. B) Diameter of neurites measured on *in vitro* slices from the same field-of-view but at different depths. The empty box plots represent measurements taken without the device covering the slice, while the filled box plots show measurements with the device in place. The boxplot whiskers indicate the 5th and 95th percentiles, and outliers are marked by the symbol ⧫[J2].

The *in vitro* images were taken of the hippocampus of a Thy1-GCaMp6f transgenic mouse. The analysis was performed using a custom MATLAB script. First, Gaussian filtering was applied to the overlapping tiles to reduce noise. Morphological operations, including *imclose*, were used to enhance neurite structures. A watershed algorithm separated detected objects, and neurites were identified based on circularity thresholds. After mapping detections back to their original coordinates, connected components were filtered by size (50–1000 pixels). Pixel-to-micron conversion enabled accurate dendrite diameter measurement. Statistical comparison of neurite diameters was performed using Student's two-sample t-test ($\alpha = 0.05$) in OriginPro. To assess the ability to image fine neuronal structures, I measured the diameter of neurites both with and without the microECoG device in place. Neurites were identified in images of hippocampal regions,

with the imaging plane aligned parallel to the neurites to maximize the number of samples detected. Figure 1.5B shows the diameters of detected neurites from the same field of view (FOV) at different depths from the slice surface. The detection algorithm identified 81 neurites in the images without the device and 112 neurites with the device. Statistical analysis revealed no significant difference in neurite diameter between the two conditions within the same FOV at a significance level of $\alpha = 0.05$.

Taken together, my results confirm that the optical performance of the transparent SMP microECoG array meets the stringent requirements for chronic multimodal experiments. This device enables the long-term integration of two-photon microscopy with cortical electrophysiology, paving the way for future studies exploring neural dynamics in healthy and diseased states.

Thesis II.2 *I demonstrated that relative intensity changes in GCaMP6f-labeled neurons relative to background fluorescence were consistently visible over 22 weeks, and no significant differences were observed during two-photon imaging of awake, freely moving mice. My results indicate that the microECoG device enables long-term stable, high-resolution multimodal imaging without significant optical signal degradation.*

To evaluate long-term optical performance, the resolution and distortion effects were assessed by analyzing changes in relative fluorescence intensity of cell bodies in *in vivo* images. Two-photon recordings (3–10 minutes) were averaged for segmentation. A MATLAB-based algorithm detected cell bodies using a roundness threshold of 0.4, excluding noise. Extracted fluorescence signals were smoothed with a Gaussian filter ($\sigma = 5$) and converted to relative inensity changes:

$$\delta F = \frac{f - f_0}{f_0} \tag{1.2}$$

where f_0 is the background fluorescence and f is the mean intensity of the cell bodies. Background fluorescence was determined from the lower 8th percentile of the image fluorescence.

Results were visualized using boxplots, with whiskers representing the 5th and 95th percentiles. Outliers were marked (⧫), and means were shown as squares (□). All figures were produced using OriginPro. Statistical comparison was performed using Student's two-sample t-test ($\alpha = 0.05$) in OriginPro.

Imaging sessions were performed at multiple time points post-implantation, spanning up to 22 weeks. Labeled neurons were visible in the first images (1-2 weeks post-implantation) and their clear contrast to the background was maintained throughout the experiment.

To quantify imaging stability, I analyzed the fluorescence intensity of automatically detected neurons relative to background fluorescence on each measurement day. For device A (gold and SIROF conductive layer), relative intensity changes remained stable across sessions, with no significant differences between measurement days (Student's t-test: $t(65) = -0.79$, $p = 0.43$) (Figure 1.6a). In contrast, device B (gold conductive layer) showed a significant variation in relative intensity across measurement days (one-way repeated analysis of variance ANOVA, OriginPro: $F(1.72, 96.15) = 16.99$, $p \ll 0.05$).

However, the mean relative intensity remained above 0.5 throughout the measurement period (Figure 1.6b).

As both devices used the same substrate material (thiol-ene/acrylate) in the optical path, I hypothesize that the observed differences in imaging performance are likely due to factors such as variations in GCaMP6f expression rather than the microECoG device itself.

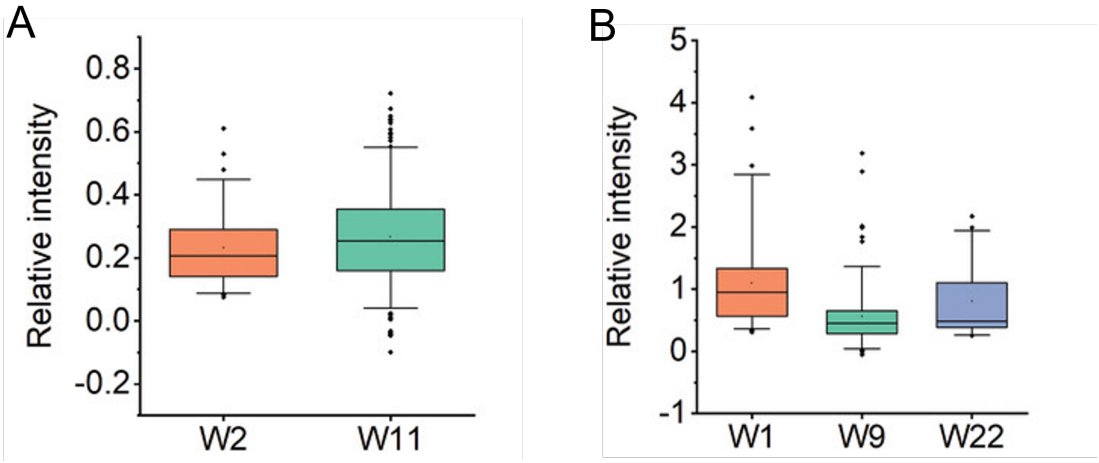

Figure 1.6: Relative intensity change measurements with microECoG A and B from two representative animals. A) Measurements with device A. Long-term two-photon relative intensity change compared to background intensity ($n_{W2} = 66; n_{W11} = 254)(n_{W2} = 66; n_{W11} = 254$). The different box plots represent measurements taken on different days. B) Measurements with device B. ($n_{W1} = 67; n_{W22} = 57$). Box plots represent different measurement days. Boxplot whiskers are $5th$ and $95th$ percentiles, and $\diamond$ are the outliers [J2].

Thesis II.3 *I conclude that SMP microECoG has reliable, long-term electrophysiological recording capabilities, including the detection of single-cell activity, for at least seven weeks, based on in vivo data.*

Transgenic adult mice (16–54 weeks old, n = 4 males, n = 3 females) expressing GCaMP6 were used. A 3 mm craniotomy was performed above the hippocampus, the overlying cortex was removed, and a thiol-ene/acrylate microelectrode was placed on the hippocampal surface, secured with a silicone-based deep brain adapter. Electrophysiological signals were recorded using the RHD2132 amplifier board (0.1 Hz–7.5 kHz bandwidth, 20 kHz sampling rate). Spike detection was performed with Kilosort3 and manually curated in Phy, classifying clusters as multi-unit (MUA) or single-unit activity (SUA) based on waveform characteristics, amplitude distribution, and auto-correlogram analysis. SpikeInterface was used to assess sorting performance via presence ratio (detecting incomplete units), inter-spike interval (ISI) violations (indicating contamination), and amplitude cutoff (measuring missed spikes). Signal-to-noise ratio and auto-correlograms were analyzed with SpikeInterface, Python, and MATLAB scripts. Waveform visualization was done with Spikes (Cortex-lab) and MATLAB, while firing rate, amplitude distribution, and spike counts were computed using MATLAB. Cell types were classified as

putative pyramidal cells, narrow-spiking, or wide-spiking interneurons based on waveform trough-to-peak time and burstiness index (BI), with a burstiness threshold of 1.2 set according to the literature.

For seven weeks, the data collected from a single animal exhibited consistent spikes, including both multi-unit and single-unit activity. To differentiate between the various cell types, putative pyramidal cells, narrow-waveform interneurons, and wide-waveform interneurons were classified based on the trough-to-peak time of the waveform and the burstiness index. The clustering exhibited an average of $24.01 \pm 7.8\%$ of cells classified as narrow-waveform interneurons, $52.15 \pm 14.63\%$ as wide-waveform interneurons, and $23.84 \pm 14.24\%$ as pyramidal cells. The mean burstiness index for the different neuron types was 1.267 ± 0.208 for narrow-waveform interneurons, 1.033 ± 0.142 for wide-waveform interneurons, and 1.426 ± 0.273 for pyramidal cells. These values indicate that pyramidal cells tend to have a higher burstiness index compared to interneurons, reflecting their well-known burst firing patterns.

Figure 1.7 shows metrics calculated on spikes, which have been extracted from a putative pyramidal cell exhibiting single-unit activity. Spike clusters recorded over seven weeks were analyzed using all available channels. The SNR was assessed throughout the recordings (Figure 1.7A). A clear trend of decreasing SNR was observed throughout the weeks. The statistical test results indicate that the majority of changes occurred during the first few weeks (weeks 1–4), likely due to biological responses and the initial development of scar tissue. In week 5, a significantly lower SNR was observed in comparison to the initial three weeks, and this diminished SNR persisted through weeks 6 and 7 (Kruskal-Wallis test: $p < 0.0001$). Figures 1.7B and 1.7C illustrate the mean amplitude and the spike rate recorded over time, respectively (Kruskal-Wallis test: $p < 0.0001$). Amplitudes in weeks 6 and 7 were significantly lower compared to weeks 1, 2, and 3. In contrast, the firing rate showed an overall increasing trend throughout the recordings, although a notably low value was observed in week 5. The firing rate in week 6 was significantly higher than in weeks 1 and 5 (Kruskal-Wallis test: $p < 0.0015$).

These features position the device as a prime candidate for future studies, particularly in fields such as epilepsy research and neurodegenerative disease drug development, where long-term electrophysiological monitoring and simultaneous calcium imaging could be crucial.

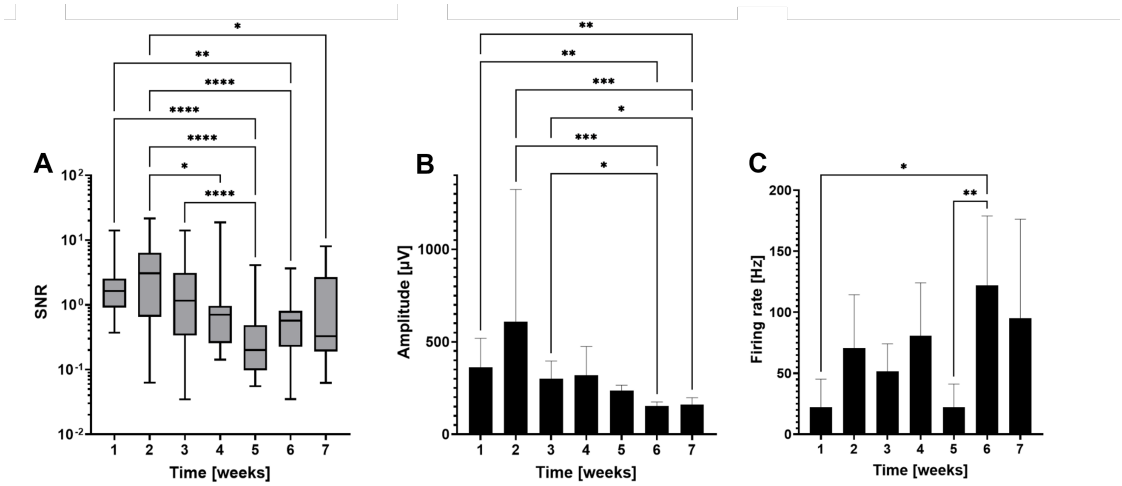

Figure 1.7: Long-term single unit recordings. A) Signal-to-noise ratio of the clusters. The box plot shows the interquartile range, which extends from the 25th to the 75th percentile, and the whiskers represent the minimum and maximum values of the data set. B) Mean amplitude of the spikes in all of the clusters during the chronic recordings. C) Number of detected clusters in the chronic recordings. Error bars represent standard deviation. (Kruskal-Wallis test: $*p < 0.05, **p < 0.01, ***p < 0.001, ****p < 0.0001$) [J3].

2 Potential applications and benefits

The findings of this research have significant implications for both fundamental neuroscience and clinical applications. The integration of multimodal recording techniques, such as combining two-photon microscopy with transparent microelectrocorticography devices, enhances our ability to study neural activity with unmatched detail. This approach enables long-term, high-resolution monitoring of neuronal populations, which is essential for understanding brain function in both healthy and diseased states.

Furthermore, the development of shape memory polymer based implants offers substantial advantages over traditional silicon-based electrodes. Their biocompatibility and reduced immune response make them ideal for long-term implantation, minimizing signal degradation and tissue damage. This opens new possibilities, for example, for brain-computer interfaces (BCIs), which rely on stable, long-term neural recordings to restore motor function in patients with paralysis or neurotrauma.

One of the primary applications of this technology is in neurodegenerative disease research. Disorders such as Alzheimer's and Parkinson's involve progressive changes in neuronal activity, synaptic dysfunction, and network disruptions. By providing stable, chronic recordings, this research supports the development of early diagnostic biomarkers and real-time tracking of disease progression. Additionally, these methods could facilitate the evaluation of novel pharmacological treatments, offering insights into their effects at the cellular and circuit levels.

Beyond multimodal recordings, this work also advances neuromodulation techniques. The study's findings on infrared neuromodulation suggest that controlled thermal stimulation can influence neuronal activity in a layer- and cell-type-specific manner. This could lead to novel therapeutic strategies for epilepsy, chronic pain management, and neuropsychiatric disorders by selectively enhancing or suppressing neural activity without invasive surgery or pharmacological side effects.

Author's list of publications

List of journal publications

[J1] **Z. Balogh-Lantos**, R. Fiáth, Á. C. Horváth, and Z. Fekete, "High density laminar recordings reveal cell type and layer specific responses to infrared neural stimulation in the rat neocortex", *Scientific Reports*, vol. 14, no. 1, p. 31 523, 2024 (cit. on pp. 4, 6–9).

[J2] Á. Szabó, M. Madarász, **Z. Lantos**, *et al.*, "Transparent thiol-ene/acrylate-based microecog devices used for concurrent recording of fluorescent calcium signals and electrophysiology in awake animals", *Advanced Materials Interfaces*, vol. 9, no. 25, p. 2 200 729, 2022 (cit. on pp. 10, 11, 13).

[J3] G. Juhász, M. Madarász, B. Szmola, *et al.*, "Hippocampal recording with a soft microelectrode array in a cranial window imaging scheme: A validation study", *Scientific Reports*, vol. 14, no. 1, p. 24 585, 2024 (cit. on pp. 10, 15).

[J4] R. Matta, **Z. Balogh-Lantos**, Z. Fekete, *et al.*, "A flexible, implantable, bioelectronic electroporation device for targeted ablation of seizure foci in the mouse brain", *Sensors*, vol. 25, no. 1, p. 4, 2024.

[J5] Á. C. Horváth, Á. Mórocz, B. Csomai, *et al.*, "Silicon optrode with a micromirror-tip providing tunable beam profile during infrared neuromodulation of the rat neocortex", *Advanced Materials Technologies*, vol. 9, no. 20, p. 2 400 044, 2024.

List of conference posters

[P1] **Z. Lantos**, R. Fiáth, C. Horváth Á, and Z. Fekete, "Intracortical effects of continuous infrared neural stimulation", 2023 (cit. on p. 4).

[P2] **Z. Balogh-Lantos**, R. Fiáth, C. Horváth Á, and Z. Fekete, "Cell- and layer-type specific intracortical effects of continuous infrared neural stimulation revealed by high-density laminar recordings in the rat neocortex", 2024 (cit. on p. 4).

[P3] **Z. Balogh-Lantos**, R. Fiáth, C. Horváth Á, and Z. Fekete, "Cell- and layer-type specific intracortical effects of continuous infrared neural stimulation revealed by high-density laminar recordings in the rat neocortex", 2024 (cit. on p. 4).

[P4] **Z. Lantos**, Á. Szabó, F. Fedor, *et al.*, "Shape memory polymer based transparent electrode array for long-term multimodal neuroimaging", 2022 (cit. on p. 10).

[P5] **Z. Lantos**, Á. Szabó, F. Fedor, *et al.*, "Shape memory polymer based transparent electrode array for long-term multimodal neuroimaging", 2022 (cit. on p. 10).

[P6] **Z. Balogh-Lantos**, R. Fiáth, C. Horváth Á, K. Kovács-Rozmer, Z. Helyes, and Z. Fekete, "Cell- and layer-specific roles of trpv1 ion channels in infrared neurostimulation: Insights from high-density laminar recordings in the mouse neocortex", 2025.

[P7] M. Madarász, **Z. Lantos**, B. Szmola, *et al.*, "Concurrent imaging of calcium signals and recording of electrophysiology in the hippocampus of awake mouse", 2023.

References

[1] P. Scheltens, K. Blennow, M. M. Breteler, *et al.*, "Alzheimer's disease", *The Lancet*, vol. 388, no. 10043, pp. 505–517, 2016 (cit. on p. 2).

[2] L. V. Kalia and A. E. Lang, "Parkinson's disease", *The Lancet*, vol. 386, no. 9996, pp. 896–912, 2015 (cit. on p. 2).

[3] R. D. Thijs, R. Surges, T. J. O'Brien, and J. W. Sander, "Epilepsy in adults", *The lancet*, vol. 393, no. 10172, pp. 689–701, 2019 (cit. on p. 2).

[4] J. Olesen, A. Gustavsson, M. Svensson, *et al.*, "The economic cost of brain disorders in europe", *European journal of neurology*, vol. 19, no. 1, pp. 155–162, 2012 (cit. on p. 2).

[5] S. D. Skaper, L. Facci, M. Zusso, and P. Giusti, "An inflammation-centric view of neurological disease: Beyond the neuron", *Frontiers in cellular neuroscience*, vol. 12, p. 72, 2018 (cit. on p. 2).

[6] R. A. Nixon and D.-S. Yang, "Autophagy and neuronal cell death in neurological disorders", *Cold Spring Harbor perspectives in biology*, vol. 4, no. 10, a008839, 2012 (cit. on p. 2).

[7] M. Nimgampalle, H. Chakravarthy, S. Sharma, *et al.*, "Neurotransmitter systems in the etiology of major neurological disorders: Emerging insights and therapeutic implications", *Ageing Research Reviews*, p. 101 994, 2023 (cit. on p. 2).

[8] Z. Fekete, Á. C. Horváth, and A. Zátonyi, "Infrared neuromodulation: A neuroengineering perspective", *Journal of Neural Engineering*, vol. 17, no. 5, p. 051 003, 2020 (cit. on p. 2).

[9] E. Albert, J. M. Bec, G. Desmadryl, *et al.*, "Trpv4 channels mediate the infrared laser-evoked response in sensory neurons", *Journal of neurophysiology*, vol. 107, no. 12, pp. 3227–3234, 2012 (cit. on p. 2).

[10] Á. C. Horváth, S. Borbély, Ö. C. Boros, *et al.*, "Infrared neural stimulation and inhibition using an implantable silicon photonic microdevice", *Microsystems & nanoengineering*, vol. 6, no. 1, p. 44, 2020 (cit. on p. 2).

[11] Á. C. Horváth, S. Borbély, F. Mihók, P. Fürjes, P. Barthó, and Z. Fekete, "Histological and electrophysiological evidence on the safe operation of a sharp-tip multimodal optrode during infrared neuromodulation of the rat cortex", *Scientific Reports*, vol. 12, no. 1, p. 11 434, 2022 (cit. on p. 2).

[12] J. L. Skousen, S. M. E. Merriam, O. Srivannavit, G. Perlin, K. D. Wise, and P. A. Tresco, "Reducing surface area while maintaining implant penetrating profile lowers the brain foreign body response to chronically implanted planar silicon microelectrode arrays", in *Progress in brain research*, vol. 194, Elsevier, 2011, pp. 167–180 (cit. on p. 3).

[13] T. Ware, D. Simon, C. Liu, *et al.*, "Thiol-ene/acrylate substrates for softening intracortical electrodes", *Journal of Biomedical Materials Research Part B: Applied Biomaterials*, vol. 102, no. 1, pp. 1–11, 2014 (cit. on p. 10).

[14] H. Eichenbaum, T. Otto, and N. J. Cohen, "The hippocampus—what does it do?", *Behavioral and neural biology*, vol. 57, no. 1, pp. 2–36, 1992.